Multiple Alignment of Spatiotemporal Deformable Objects for the Average-Organ Computation

Shun Inagaki[1], Hayato Itoh[1], and Atsushi Imiya[2(✉)]

[1] Graduate School of Advanced Integration Science, Chiba University, Yayoi-cho 1-33, Inage-ku, Chiba 263-8522, Japan
[2] Institute of Management and Information Technologies, Chiba University, Yayoi-cho 1-33, Inage-ku, Chiba 263-8522, Japan
imiya@faculty.chiba-u.jp

Abstract. We deal with multiple image warping, which computes deformation fields between an image and a collection of images, as an extension of variational image registration. Using multiple image warping, we develop a variational method for the computation of average images of biological organs in three-dimensional Euclidean space. The average shape of three-dimensional biological organs is an essential feature to discriminate abnormal organs from normal organs. There are two kinds of volumetric image sets in medical image analysis. The first one is a collection of static volumetric data of an organ and/or organs. The other is a collection of temporal volumetric data of an organ and/or organs. A collection of temporal volumetric beating hearts is an example of temporal volumetric data. For spatiotemporal volumetric data, we can compute (1) the temporal average, which is the average of a heart during a cycle, (2) the frame average, which is the average of hearts at a frame, and (3) the temporal average of frame averages.

1 Introduction

In this paper, we deal with multiple image warping, which computes deformation fields between an image and a collection of images. This collection of multiple deformation fields provides the average image and shape of a collection of volumetric images and objects.

In medical diagnosis, the average shape of individual organs provides essential properties for the general expression of organs [20]. In computational anatomy, the statistical average shape, which is computed using principal component analysis of a shape descriptor, is well defined [12].

There are two kinds of volumetric image sets in medical image analysis. The first one is a collection of static volumetric data of an organ. The other is a collection of temporal volumetric data of an organ. A sequence of images of beating volumetric hearts is an example of temporal volumetric data. For spatiotemporal volumetric data, we can compute (1) the temporal average, which is the average of a heart during a cycle, (2) the frame average, which is the

L. Agapito et al. (Eds.): ECCV 2014 Workshops, Part IV, LNCS 8928, pp. 353–366, 2015.
DOI: 10.1007/978-3-319-16220-1_25

average of hearts at a frame, and (3) the temporal average of frame averages. The first, second and third averages derive the standard shape of the organ of a human, the standard shape of a frame of beating hearts and the standard shape of a collection of beating hearts, respectively. Therefore, the second average detects abnormalities of a heart from a collection of hearts. Moreover, the third average derives a standard static heart for computational anatomy.

2 Related Works

In both structure pattern recognition [9,19] and variational registration [20], the average shape among a collection of given shapes is of interest. Some pioneering works demonstrated a registration process achieved by pattern matching based on dynamic programming [22,23], which is a fundamental idea in pattern recognition. These approaches involve the matching and retrieval of occluded shapes, and they are intended for the global alignment of planar shapes.

The shape-matching algorithm observes a collection of given shapes, detects the contours and then computes (1) distances among them and (2) point correspondences between the contours [10]. However, it tends to be less accurate in the representation of local structures because the point correspondences are computed without preserving the geometric local structure of the shapes. In structure pattern recognition [9,19], the average of a collection of combinatorial structures such as strings and graphs is of interest. Multiple alignment of strings, which is achieved by dynamic programing, is a fundamental tool for motif search in bioinformatics. For multiple alignment of volumetric data, we apply variational method, since these data are not expressed as strings.

Warping and morphing are fundamental techniques in computer graphics to interpolate and generate shapes and objects. In medical applications, morphing is used for the description of the deformation process of biological organs. This process predicts the deformable motion of biological organs in the human torso such as the beating heart, and the deformation of lungs during breathing. In medical image diagnosis and retrieval [2,20], average images and shapes of individual organs provide essential properties for the general expression of organs. Shape retrieval categorises and classifies shapes, and finds shapes from portions of shapes. In shape retrieval, the matching of shapes based on the diffeomorphism of shapes [5,6] and the descriptor of shape boundary contours [10] are used. In the matching process for discrete shapes, the string edit distance [7,9] computed by dynamic programming is a fundamental tool. Moreover, in the matching process of images, the variational registration strategy [2,3,20] is a typical tool. In computational anatomy, the statistical average shape, which is computed using principal component analysis of the shape descriptor, is well defined [11,12]. In both structure pattern recognition [7,8] and variation registration [4,20], the average shape of a collection of given shapes is of interest.

There are various methods for computing the average shape [4,21]. These methods are based on the mathematical definition that shapes are the boundary contours of physical objects [13,14]. This definition is suitable for dealing with

highly nonlinear geometric variations. Furthermore, in the comparative reading of medical images, image registration is the main method used to classify the differences among the images. In particular, the establishment of local deformations between a collection of given shapes has attracted researchers of medical image analysis for decades.

3 Variational Average Computation

We define a variational average image g of volumetric images $\{f_i\}_{i=1}^m$ in the three-dimensional Euclidean space $\mathbf{R}^3$ as the minimiser of the variational problem

$$J(\{\boldsymbol{u}_k\}_{k=1}^m) = \sum_{k=1}^m \int_{\mathbf{R}^3} (g(\boldsymbol{x}-\boldsymbol{u}_k) - f_k(\boldsymbol{x}))^2 d\boldsymbol{x} + \lambda \int_{\mathbf{R}^3} |\nabla g|^2 d\boldsymbol{x} + \mu \sum_{k=1}^m \int_{\mathbf{R}^3} |\nabla \boldsymbol{u}_k|^2 d\boldsymbol{x} + \sigma \int_{\mathbf{R}^3} \left(\sum_{k=1}^m \boldsymbol{u}_k \right)^2 d\boldsymbol{x} \tag{1}$$

where

$$\Gamma = \int_{\mathbf{R}^3} |\nabla g|^2 d\boldsymbol{x},\ U_k = \int_{\mathbf{R}^3} |\nabla \boldsymbol{u}_k|^2 d\boldsymbol{x},\ S = \sum_{k=1}^m \boldsymbol{u}_k, \tag{2}$$

are regularisers for g and deformation fields $\{\boldsymbol{u}_k\}_{k=1}^n$. The constraints Γ and U_k imply that the average g and the deformation fields are smooth, respectively. The constraint S implies that the average image exists at the median point of the deformation fields. We set the solution of the variational problem of eq. (1) as

$$g = \mathrm{VA}_k(\{f_k\}_{k=1}^m). \tag{3}$$

For a collection of spatiotemporal functions $\{h_i(\boldsymbol{x},t)\}_{i=1}^m$ defined in the interval $0 \le t \le T$, we define a collection of temporally sampled data as

$$h_{ij}(\boldsymbol{x}) = h_i(\boldsymbol{x},(j-1)\Delta), i = 1,2,\cdots,m,\ j = 1,\cdots,n \tag{4}$$

for $(n-1)\Delta = T$. For $\{h_{ij}\}_{i=1\,j=1}^{m\,n}$, we define a pair of collections of averages as

$$\{g_i(\boldsymbol{x})\}_{i=1}^m = \mathrm{VA}_j(\{h_{ij}\}_{i=1\,j=1}^{m\,n}),\ \{g(\boldsymbol{x},j)\}_{j=1}^n = \mathrm{VA}_i(\{h_{ij}\}_{i=1\,j=1}^{m\,n}). \tag{5}$$

Here, $g_i(\boldsymbol{x})$ and $g(\boldsymbol{x},j_0)$ are the temporal average of a sequence $h_i(\boldsymbol{x},t)$ and the frame average of $h_i(\boldsymbol{x},j_0\Delta)$ for a fixed j_0 such that $1 \le j \le n$, respectively.

Moreover, these two averages derive

$$\overline{g}(\boldsymbol{x}) = \mathrm{VA}_i(\{g_i\}_{i=1}^m),\ \underline{g}(\boldsymbol{x}) = \mathrm{VA}_j(\{g(\boldsymbol{x},j)\}_{j=1}^n). \tag{6}$$

Here, $\overline{g}$ and $\underline{g}$ is the spatial average of the temporal averages and the temporal average of the spatial averages, respectivly. Figure 1 shows the relations among these four averages for temporal volumetric image data. For these two averages $\overline{g}$ and $\underline{g}$, we have the following property.

Property 1. *The spatial average of the temporal averages $\overline{g}$ and the temporal average of the spatial averages $\underline{g}$ generally satisfy the irequality $\overline{g}(\boldsymbol{x}) \neq \underline{g}(\boldsymbol{x})$.*

This property implies that the order of operations for average computation affects the results.

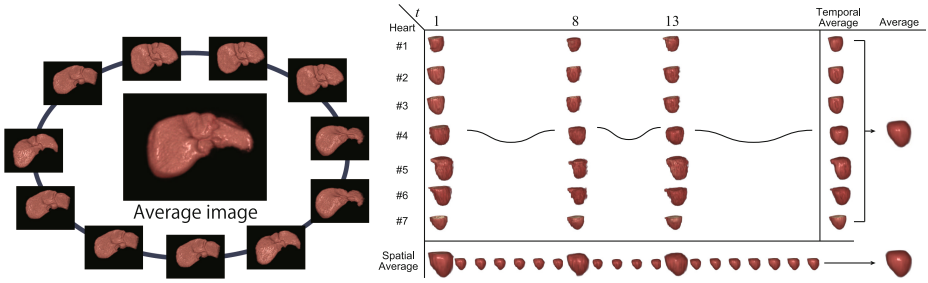

(a) Spatial average (b) Temporal average

Fig. 1. Average image. (a) The average shape of usual organs is computed by the uni-step method. (b) The average shape of temporal organs, such as beating hearts, is computed by the bi-step method. First, we compute the temporal average of an organ. Then, the spatial average is computed from individual temporal averages.

4 Fast Numerical Computation

We derive a numerical method for solving eq. (1). From eq. (1), for the variational average image g and deformation fields $\boldsymbol{u}_k$ we derive the Euler-Lagrange equations

$$\alpha \Delta g(\boldsymbol{x}) - G = 0, \quad \beta \Delta \boldsymbol{u}_k(\boldsymbol{x}) - U_k = 0, \tag{7}$$

where

$$G = \sum_{k=1}^{m} (g(\boldsymbol{x}) - f_k(\boldsymbol{x} - \boldsymbol{u}_k)), \tag{8}$$

$$U_k = \gamma(\sum_{k=1}^{m} \boldsymbol{u}_k + (g(\boldsymbol{x}) - f_k(\boldsymbol{x} - \boldsymbol{u}_k))\nabla(g(\boldsymbol{x}) - f_k(\boldsymbol{x} - \boldsymbol{u}_k))). \tag{9}$$

Next, we convert the elliptic partial differential equations in eq. (7) to the diffusion equations

$$\frac{\partial g}{\partial t} = \Delta g(\boldsymbol{x}) - \frac{1}{\alpha} G, \quad \frac{\partial \boldsymbol{u}_k}{\partial t} = \Delta \boldsymbol{u}_k(\boldsymbol{x}) - \frac{1}{\beta} U_k, \tag{10}$$

and discretise them as

$$\frac{g^{(n+1)} - g^{(n)}}{\tau} = \boldsymbol{L} g^{(n+1)} - \frac{1}{\alpha} G^{(n)}, \tag{11}$$

$$\frac{\boldsymbol{u}_k^{(n+1)} - \boldsymbol{u}_k^{(n)}}{\tau} = \boldsymbol{L} \boldsymbol{u}_k^{(n+1)} - \frac{1}{\beta} U_k^{(n)}, \tag{12}$$

where $\boldsymbol{L}$ is the discrete Laplacian operation. Therefore, we obtain the iteration forms [18]

$$(\boldsymbol{I} - \tau \boldsymbol{L}) g^{(n+1)} = g^{(n)} - \frac{\tau}{\alpha} G^{(n)}, \tag{13}$$

$$(\boldsymbol{I} - \tau \boldsymbol{L}) \boldsymbol{u}_k^{(n+1)} = \boldsymbol{u}_k^{(n)} - \frac{\tau}{\beta} U_k^{(n)}. \tag{14}$$

For three-dimensional problems, $\boldsymbol{L}$ are described as

$$\boldsymbol{L} = \boldsymbol{D} \otimes \boldsymbol{I} \otimes \boldsymbol{I} + \boldsymbol{I} \otimes \boldsymbol{D} \otimes \boldsymbol{I} + \boldsymbol{I} \otimes \boldsymbol{I} \otimes \boldsymbol{D}, \tag{15}$$

for

$$\boldsymbol{D} = \begin{pmatrix} -1 & 1 & 0 & \cdots & 0 & 0 & 0 \\ 1 & -2 & 1 & \cdots & 0 & 0 & 0 \\ 0 & 1 & -2 & \cdots & 0 & 0 & 0 \\ \vdots & \vdots & \vdots & \ddots & \vdots & \vdots & \vdots \\ 0 & 0 & 0 & \cdots & 1 & -2 & 1 \\ 0 & 0 & 0 & \cdots & 0 & 1 & -1 \end{pmatrix}, \tag{16}$$

where $\boldsymbol{A} \otimes \boldsymbol{B}$ is the Kronecker product of matrices $\boldsymbol{A}$ and $\boldsymbol{B}$, assuming the von-Neumann condition on the boundary. The eigenvalues of $\boldsymbol{D}$ are $\lambda_k = -4 \sin^2 \frac{\pi k}{2M}$ for the $M \times M$ matrix [17], and the eigenmatrix [16] of $\boldsymbol{D}$, is

$$\boldsymbol{\Phi} = \left(\left(\epsilon \cos \frac{(2j+1)i}{2\pi} \pi M \right) \right), \ \epsilon = \begin{cases} 1 & \text{if } j = 0 \\ \frac{1}{\sqrt{2}} & \text{otherwise.} \end{cases} \tag{17}$$

$\boldsymbol{\Phi}$ is the matrix of the DCT-II transform. Therefore, the matrix $\boldsymbol{L}$ is decomposed as

$$\begin{aligned} \boldsymbol{L} &= (\boldsymbol{\Phi} \otimes \boldsymbol{\Phi} \otimes \boldsymbol{\Phi})(\boldsymbol{\Lambda} \otimes \boldsymbol{I} \otimes \boldsymbol{I} + \boldsymbol{I} \otimes \boldsymbol{\Lambda} \otimes \boldsymbol{I} + \boldsymbol{I} \otimes \boldsymbol{I} \otimes \boldsymbol{\Lambda})(\boldsymbol{\Phi} \otimes \boldsymbol{\Phi} \otimes \boldsymbol{\Phi})^\top \\ &= \boldsymbol{U} \boldsymbol{\Sigma} \boldsymbol{U}^\top \end{aligned} \tag{18}$$

and the eigenvalues of $\boldsymbol{L}$ are $\lambda_i + \lambda_j + \lambda_k$.

In each step of the iteration, the results are expressed on the Euler frame. Images sampled by the Lagrange frame do not guarantee correspondence between points. Therefore, we resample the results using the Lagrange frame [1]. In the Lagrange-frame-sampled images, we use Delaunay-triangle-based interpolation [1] since the method satisfies the minimum gradient property.

Setting $\boldsymbol{g}^{(n)}$ to be the vector expression of the sampled $g^{(n)}$, we have the iteration form

$$\boldsymbol{g}^{(n+1)} = \boldsymbol{U} \boldsymbol{M}^n \boldsymbol{U}^\top (1 - \frac{m\tau}{\alpha}) \boldsymbol{g}^{(1)} + \boldsymbol{b}^{(n)}, \tag{19}$$

where $\boldsymbol{b}^{(n)} = \sum_{k=1}^{m} \frac{\tau}{\alpha} f_k(\boldsymbol{x} - \boldsymbol{u}_k^{(n))})$. For sufficiently large n, we can replace $\boldsymbol{b}^{(n)}$ with a constant vector $\boldsymbol{c}$. Therefore, we analyse the convergence condition of

$$\boldsymbol{g}^{(n+1)} = \boldsymbol{U} \boldsymbol{M}^n \boldsymbol{U}^\top (1 - \frac{m\tau}{\alpha}) \boldsymbol{g}^{(1)} + \boldsymbol{c}, \tag{20}$$

[1] There are two reference frames, the Euler frame and Lagrange frame [3]. When we have an image B and an invertible transform φ, the frames are described as $B^{Lagrange}(\varphi(i,j,k)) := B(i,j,k)$ and $B^{Euler}(i,j,k) := B(\varphi^{-1}(i,j,k))$.

where $\boldsymbol{c}$ is a constant vector with the property $|\boldsymbol{c}-\boldsymbol{b}^{(N)}| < \varepsilon \ll 1$ for a sufficiently large integer N.

Since the matrix $\boldsymbol{U}$ is a unitary matrix, the convergence property of the algorithm depends on the spectral radius of the matrix $\boldsymbol{M}$. Therefore, $\boldsymbol{g}^{(n)}$ converges if the relation

$$\max\left(\left|\frac{1}{1-\tau(\lambda_i+\lambda_j+\lambda_k)}\left(1-\frac{m\tau}{\alpha}\right)\right|\right) < 1, \tag{21}$$

is satisfied for $0 < \alpha$, $0 < \tau$ and $0 < m$. The inequality $-12 < (\lambda_i+\lambda_j+\lambda_k) \leq 0$ implies that the value of $\frac{1}{1-\tau(\lambda_i+\lambda_j+\lambda_k)}$ becomes maximum for $\lambda_i+\lambda_j+\lambda_k = 0$. Therefore, from the inequality

$$\max\left(\left|\left(1-\frac{m\tau}{\alpha}\right)\right|\right) < 1, \tag{22}$$

for $-1 < 1-\frac{m\tau}{\alpha} < 1$, if $\tau < \frac{2\alpha}{m}$ is satisfied, the iteration form converges to the unique solution.

For the computation of $\boldsymbol{u}_k$, setting $|\boldsymbol{d} - \frac{\tau}{\beta}(\gamma\sum_{j=1,j\neq k}^{m}\boldsymbol{u}_j^{(N)})| < \varepsilon \ll 1$ for a sufficiently large N, we have the relation

$$\boldsymbol{u}_k^{(n+1)} = \left(1-\frac{(1+\epsilon)\gamma\tau}{\beta}\right)\boldsymbol{U}\boldsymbol{M}^n\boldsymbol{U}^\top\boldsymbol{u}_k^{(n)} + \boldsymbol{d}, \tag{23}$$

where ϵ is a small perturbation caused by warping of data in each step of the iteration. The spectral radius of the matrix $\left(1-\frac{(1+\epsilon)\gamma\tau}{\beta}\right)\boldsymbol{U}\boldsymbol{M}^n\boldsymbol{U}^\top$ derives the convergence condition,

$$\max\left(\left|\frac{1}{1-\tau(\lambda_i+\lambda_j+\lambda_k)}\left(1-\frac{\tau(1+\epsilon)\gamma}{\beta}\right)\right|\right) < 1. \tag{24}$$

Equation (24) leads to the convergence condition $\tau < \frac{2\beta}{(1+\epsilon)\gamma}$.

5 Numerical Examples

For numerical examples we computed averages of seven hearts with 20 frames. These images show renders surfaces of volumetric grey valued images in the three dimensional Euclidean space. The numerical results show the rendered surfaces. The resolution of each volumetric heart is Grey-value × Horizontal × Vertical × Depth = $256 \times 128 \times 128 \times 15$. In total, the size of data is $256 \times 128 \times 128 \times 15 \times 20 \times 7$. Figures 2 and 3 show 20 frames of temporal volumetric images a couple of beating heart sequences. These figures show that shapes f heart depend on the frames and individuals.

We evaluate the warp image error WIE, the total deformation norm FNS, the volume V_i and the deformation energy DE_k which are defined as

$$\mathrm{WIE}(\boldsymbol{x}) = \int_{\mathbf{R}^3} \|g(\boldsymbol{x}) - f_i(\boldsymbol{x} - \boldsymbol{u}_k)\|_2 d\boldsymbol{x}, \tag{25}$$

$$\mathrm{FNS}(\boldsymbol{x}) = \|\sum_{i=1}^{n} \boldsymbol{u}_i\|_2, \tag{26}$$

$$V_k = \int_{\mathbf{R}^3} f_k(\boldsymbol{x} - \boldsymbol{u}_k) d\boldsymbol{x}, \tag{27}$$

$$DE_k = \int_{\mathbf{R}^3} ||\boldsymbol{u}_k(\boldsymbol{x})||_2^2 d\boldsymbol{x}. \tag{28}$$

For the numerical computation, we adopt the regularisation parameters $\alpha = 10^{-1}$, $\beta = 10^2$ and $\gamma = 10^4$.

Figures 4 (a), (b) and (c) show rendered shapes of the spatial average of the temporal averages, the eigenorgan of the temporal averages and the arithmetic average with respect to time, respectively. For the eigenorgan, see Appendix. Figures 4 (b), (d) and (f) show radar charts of the total deformation norms of cycle of a volumetric beating-heart for the variational temporal average, the temporal eigenorgan and the arithmetic average with respect to time, respectively.

In the radar charts, 20 frames of a volumetric beating-heart sequence are shown on the circle and the arrow from the origin of the circle is the deformation energy required to deform the temporal average, which is shown in the centre of the chart, to the volumetric image at each frame. The arrows show the total difference between the average and each shape on the circle. These charts show that the variational average is a stable shape with respect to the cyclic deformation because the deformations on the chart are symmetric. However, the eigenorgan of the beating volumetric heart is unstable against cyclic motion because the deformation on the chart is asymmetric.

Figures 5(a) and (b) show the total of deformation norms and the warp image errors, respectively for the three averages.

Figures 6(a) and (b) show the spatial average of the temporal averages of the seven beating hearts. and the eigenorgan of the temporal averages of the seven beating volumetric hearts, respectively. The boundary of the spatial average of the temporal averages is smooth, although that of the eigenorgan contains small vibrations. These results show the variational average of the variational temporal averages is suitable for the construction of the model of the stationary heart of a human. Figure 6(c) shows the graphical expression of multidimensional scaling of 7 hearts. Figure 6(c) shows the graphical expression of multidimensional scaling of 7 hearts. This graph clarifies that both averages exist in a neighbour area of the median shape.

6 Validation of the Results

Tables 1 and 2 evaluate the WIE and FN, respectively, of temporal average of a volumetric beating-heart sequence. Tables 3 and 4 evaluate the WIE and

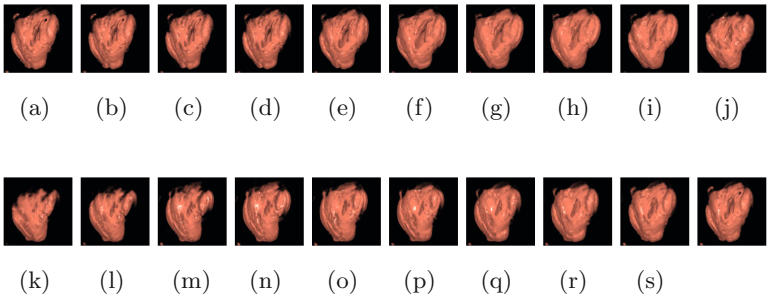

Fig. 2. Sequence of volumetric beating-heart images I. (a)-(t) are a sequence of 20 input temporal images. These images show renders surfaces of volumetric grey valued images in the three dimensional Euclidean space.

FN, respectively, of spatial average of volumetric beating-hearts of a frame 20 sequences. These results show that our method achieves multiple alignment of temporal volumetric data for the computation of the average of a beating-heart image sequence and the temporal average of beating-heart sequence occupies the mean region of a volumetric beating-heart sequence, respectively.

Figure 8 shows the distance between the average heart and each frame of seven hearts for arithmetic average, eigenorgan and variational average computed by the proposed method, respectively. For the distance between a pair of volumetric images, see Appendix. In this figure, the top, middle and bottom rows are the temporal arithmetic average, the temporal eigenorgan and the temporal variational average, respectively. Figures 9(a) and 9(b) show radar charts of the spatial temporal averages and the temporal spatial averages of a collection of heart sequences, respectively. In these evaluations, the volumetric centroids of the average and each frame are aligned as the pre-processing

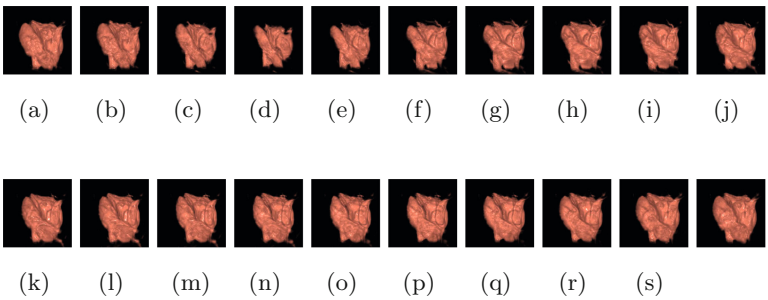

Fig. 3. Sequence of volumetric beating-heart images II. (a)-(t) are a sequence of 20 input temporal images. These images show renders surfaces of volumetric grey valued images in the three dimensional Euclidean space.

Table 1. WIE of each heart

data number		1	2	3	4	5	6	7
arithmetic average	average	1.326	1.950	2.111	2.699	3.250	2.284	1.505
	variance	0.045	0.160	0.142	0.191	0.322	0.139	0.036
eigenorgan	average	1.522	2.434	2.706	3.236	4.102	2.826	1.774
	variance	0.507	1.368	1.047	1.000	4.296	1.172	0.966
variational average	average	0.622	1.090	1.069	1.555	1.891	0.529	0.631
	variance	0.008	0.050	0.027	0.095	0.133	0.010	0.008

Table 2. FIN of individual heart

data number	1	2	3	4	5	6	7
average of deformation vector norms	0.014	0.022	0.031	0.028	0.043	0.146	0.015
variance of deformation vector norms	0.000	0.000	0.000	0.000	0.000	0.001	0.000
deformation energy	0.000	0.001	0.001	0.001	0.001	0.002	0.000

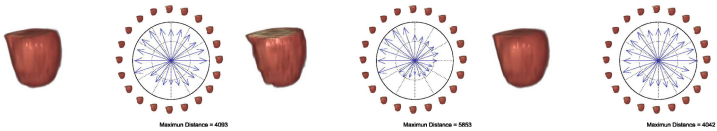

(a) (b) (c) (d) (e) (f)

Fig. 4. Comparison of the three averages of a beating heart. (a) Arithmetic average of a beating-heart sequence. (b) Radar chart of the total deformation norms for the arithmetic average. (c) Eigenorgan of a beating-heart sequence. (d) Radar chart of the total deformation norms for the eigenorgan of a sequence of a beating heart. (e) Variational average of a beating-heart sequence. (f) Radar chart of the total deformation norms for the variational temporal average of a beating heart. In the radar charts, 20 frames of a volumetric beating-heart sequence are shown on the circle and the arrow from the origin of the circle is the deformation energy required to deform the temporal average, which is shown in the centre of the chart, to the volumetric image at each frame. The arrows show the total difference between the average and each shape on the circle.

In the radar charts, the arrows show the volumetric difference between the average at the centre and each frame of motion. The variational temporal average processes geometrical properties that the difference between the average and each frame expresses the geometrical and volumetric differences caused by deformation in a beating-heart sequence.

Table 3. WIE for frames

data number		1	2	3	4	5	6	7	8	9	10
arithmetic average	average	6.251	6.092	5.975	5.502	5.085	4.736	4.252	4.223	4.051	4.351
	variance	1.575	1.433	0.785	0.431	0.396	0.336	0.356	0.607	0.759	1.141
eigenorgan	average	10.700	10.488	10.125	9.303	8.626	8.006	7.182	6.869	6.802	7.247
	variance	14.230	13.814	13.104	11.065	10.178	7.922	4.868	5.429	6.220	8.269
variational average	average	2.672	2.671	2.576	2.331	2.180	2.111	1.999	1.900	1.876	1.996
	variance	0.264	0.300	0.249	0.163	0.174	0.143	0.136	0.150	0.150	0.188
data number		11	12	13	14	15	16	17	18	19	20
arithmetic average	average	4.762	5.109	5.309	5.461	6.058	6.318	6.433	6.620	6.627	6.496
	variance	1.329	1.483	1.523	1.326	1.344	1.544	1.978	2.103	1.795	1.496
eigenorgan	average	8.124	9.670	9.060	9.591	10.227	10.804	11.197	11.226	10.979	10.679
	variance	9.639	8.846	12.372	13.613	14.197	15.423	16.549	17.201	15.505	14.022
variational average	average	2.166	2.357	2.368	2.402	2.527	2.565	2.697	2.778	2.795	2.750
	variance	0.208	0.238	0.244	0.221	0.205	0.252	0.347	0.375	0.327	0.239

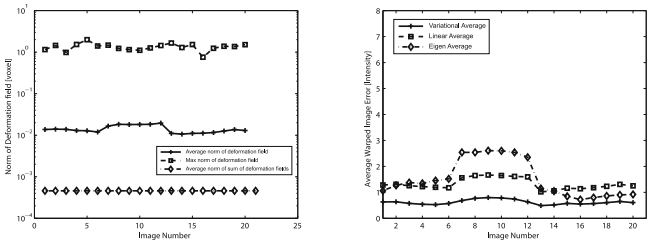

(a) (b)

Fig. 5. Comparison of the three averages for a beating-heart sequence. (a) Total deformation norms $\mathrm{FNS}(\boldsymbol{x}) = \| \sum_{i=1}^{m} \boldsymbol{u}_i \|_2$. (b) Warp errors $\mathrm{WIE}(\boldsymbol{x}) = \|g(\boldsymbol{x}) - f_i(\boldsymbol{x} - \boldsymbol{u}_i)\|_2$.

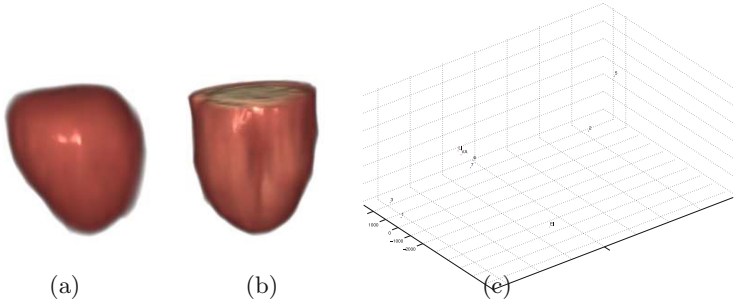

(a) (b) (c)

Fig. 6. Comparison of the averages of a beating heart. (a) Spatial average of the temporal averages of 7 beating hearts. (b) Eigenorgan of the temporal averages of 7 beating hearts. (c) The graphical MDS of two types of variational averages.

Table 4. FEN of the spatial averages

frame number	1	2	3	4	5	6	7	8	9	10
average of deformation vector norms	0.162	0.164	0.158	0.149	0.136	0.119	0.108	0.107	0.104	0.115
variance of deformation vector norms	0.002	0.001	0.001	0.000	0.000	0.000	0.000	0.001	0.001	0.001
deformation energy	0.002	0.002	0.002	0.002	0.002	0.002	0.002	0.002	0.002	0.002
frame number	11	12	13	14	15	16	17	18	19	20
average of deformation vector norms	0.129	0.141	0.150	0.148	0.164	0.172	0.173	0.175	0.174	0.169
variance of deformation vector norms	0.001	0.001	0.001	0.001	0.001	0.001	0.002	0.002	0.002	0.001
deformation energy	0.002	0.002	0.002	0.002	0.003	0.003	0.003	0.003	0.003	0.003

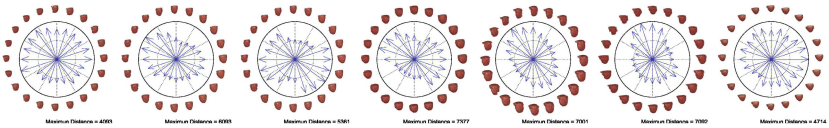

(a) heart1 (b) heart2 (c) heart3 (d) heart4 (e) heart5 (f) heart6 (g) heart7

Fig. 7. Distances between arithmetic average heart and inputs

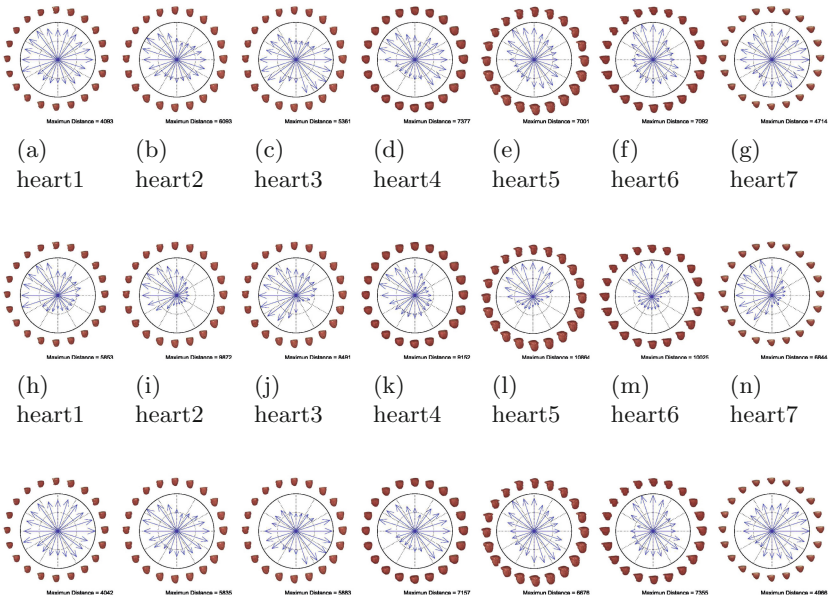

(a) heart1 (b) heart2 (c) heart3 (d) heart4 (e) heart5 (f) heart6 (g) heart7

(h) heart1 (i) heart2 (j) heart3 (k) heart4 (l) heart5 (m) heart6 (n) heart7

(o) heart1 (p) heart2 (q) heart3 (r) heart4 (s) heart5 (t) heart6 (u) heart7

Fig. 8. Distance between the average heart and inputs. Top, middle and bottom rows are the temporal arithmetic average, the temporal eigenorgan and the temporal variational average, respectively.

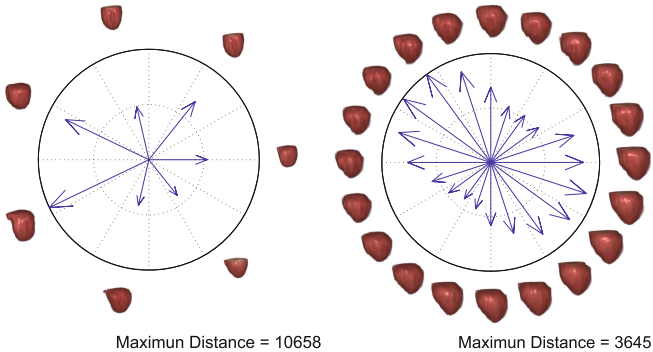

(a) Average of the temporal averages (b) Average of the spatial averages

Fig. 9. Spatial temporal averages and temporal spatial averages of a collection of heart sequences

7 Conclusions

Using multiple image warping, which computes deformation fields between an image and a collection of images, we developed a variational method for the computation of the average images and the average shapes of both static and temporal biological organs in three-dimensional Euclidean space. We combined the diffusion registration technique and optical-flow computation for the computation of spatial deformation field between the average image and input organs.

For spatiotemporal volumetric data, (1) the temporal average is the average of a heart during a cycle, (2) the frame average is the average of hearts at a frame, and (3) the temporal average of frame averages. The first, second and third averages derive the standard shape of the organ of a human, the standard shape of a frame of beating hearts and the standard shape of a collection of beating hearts, respectively.

This research was supported by the "Computational Anatomy for Computer-Aided Diagnosis and Therapy: Frontiers of Medical Image Sciences" and "Multidisciplinary Computational Anatomy and Its Application to Highly Intelligent Diagnosis and Therapy" projects funded by a Grant-in-Aid for Scientific Research on Innovative Areas from MEXT, Japan, and by Grants-in-Aid for Scientific Research funded by the Japan Society for the Promotion of Science.

Appendix

Let

$$\int_{\mathbf{R}^3} f^2 d\boldsymbol{x} \leq \infty$$

for a function $f(\boldsymbol{x})$ defined on $\mathbf{R}^3$. Since

$$f(\boldsymbol{x}+\boldsymbol{\delta}) = f(\boldsymbol{x}) + \boldsymbol{\delta}^\top \nabla f$$

and

$$\int_{\mathbf{R}^3} f f_x d\boldsymbol{x} = 0,\ \int_{\mathbf{R}^3} f_x f_y d\boldsymbol{x} = 0,\ \int_{\mathbf{R}^3} f f_y d\boldsymbol{x} = 0,$$
$$\int_{\mathbf{R}^3} f_y f_z d\boldsymbol{x} = 0,\ \int_{\mathbf{R}^3} f f_z d\boldsymbol{x} = 0,\ \int_{\mathbf{R}^3} f_z f_x d\boldsymbol{x} = 0$$

in the neighbourhood of the point $\boldsymbol{x}$, the local dimension of the volumetric-image space is four. Therefore, using the local orthogonal base, the volumetric eigenimage is expressed as

$$f(\boldsymbol{x}) = \sum_{k=1}^{4} \alpha_k \boldsymbol{u}_k(\boldsymbol{x}),$$

where $\{\boldsymbol{u}_i\}_{i=1}^4$ are the first four principal components of the covariance kernel $K(\boldsymbol{x},\boldsymbol{y}) = \sum_{i=1}^n f(\boldsymbol{x}) f(\boldsymbol{y})$.

Setting

$$f_a(\boldsymbol{x}) = \frac{1}{n}\sum_{i=1}^{n} f_i(\boldsymbol{x}-\boldsymbol{g}_i),\ \boldsymbol{g}_i = \frac{1}{\Omega}\int_{\mathbf{R}^3} f_i(\boldsymbol{x}) d\boldsymbol{x}$$

the volumetric distance is computed as

$$D(f,g) = \min_{\boldsymbol{R}} \int_{\mathbf{R}^3} |f_a(\boldsymbol{x}) - g_a(\boldsymbol{R}\boldsymbol{x})|^2 d\boldsymbol{x}.$$

References

1. Hjelle, Ø., Dæhlen, M.: Triangulations and Applications. Mathematics and Visualization Series. Springer (2006)
2. Fischer, B., Modersitzki, J.: Ill-posed medicine- an introduction to image registration. Inverse Prob. **24**, 1–17 (2008)
3. Modersitzki, J.: Numerical Methods for Image Registration, OUP (2004)
4. Rumpf, M., Wirth, B.: A nonlinear elastic shape averaging approach. SIAM J. Imaging Sci. **2**, 800–833 (2009)
5. Arrate, F., Ratnanather, J.T., Younes, L.: Diffeomorphic active contours. SIAM J. Imaging Sci. **3**, 176–198 (2010)
6. Sharon, E., Mumford, D.: 2D-shape analysis using conformal mapping. IJCV **70**, 55–75 (2006)
7. Sebastian, T.B., Klein, P.N., Kimia, B.B.: On aligning curves. IEEE PAMI **25**, 116–125 (2003)
8. Baeza-Yates, R., Valiente, G.: An image similarity measure based on graph matching. In: Proc. 7th Int. Symp. String Processing and Information Retrieval, pp. 8–38 (2000)
9. Riesen, K., Bunke, H.: Approximate graph edit distance computation by means of bipartite graph matching. Image Vision Comput. **27**, 950–959 (2009)

10. Tanase, M., Veltkamp, R.C., Haverkort, H.J.: Multiple polyline to polygon matching. In: Deng, X., Du, D.-Z. (eds.) ISAAC 2005. LNCS, vol. 3827, pp. 60–70. Springer, Heidelberg (2005)
11. Stegmann, M.B., Gomez, D.D.: A brief introduction to statistical shape analysis, Informatics and Mathematical Modelling, Technical University of Denmark (2002). http://www2.imm.dtu.dk/pubdb/p.php?403
12. Srivastava, A., Joshi, S., Mio, W., Liu, X.: Statistical shape analysis: Clustering, learning, and testing. IEEE PAMI **27**, 590–602 (2005)
13. Rumpf, M., Wirth, B.: An elasticity-based covariance analysis of shapes. IJCV **92**, 281–295 (2011)
14. Wirth, B., Bar, L., Rumpf, M., Sapiro, G.: A continuum mechanical approach to geodesics in shape space. IJCV **93**, 293–318 (2011)
15. Strang, G.: Computational Science and Engineering. Wellesley-Cambridge Press (2007)
16. Strang, G., Nguyen, T.: Wavelets and Filter Banks. Wellesley-Cambridge Press (1996)
17. Demmel, J.W.: Applied Numerical Linear Algebra. SIAM (1997)
18. Varga, R.S.: Matrix Iterative Analysis, 2nd edn. Springer (2000)
19. Sebastian, T.B., Klein, P.N., Kimia, B.B.: On aligning curves. IEEE PAMI **25**, 116–125 (2003)
20. Hill, D.L.G., Batchelor, P.G., Holden, M., Hawkes, D.J.: Medical image registration. Physics in Medicine and Biology **46**, R1–45 (2001)
21. Avants, B., Gee, J.C.: Geodesic estimation for large deformation anatomical shape averaging and interpolation. NeuroImage **23**, S139–S150 (2004)
22. Milios, E., Petrakis, E.G.M.: Shape retrieval based on dynamic programming. IEEE IP **9**, 141–147 (2000)
23. Grigorescu, C., Petkov, N.: Distance sets for shape filters and shape recognition. IEEE IP **12**, 1274–1286 (2003)